Area-Preserving Mapping of 3D Carotid Ultrasound Images Using Density-Equalizing Reference Map

Gary P. T. Choi, Bernard Chiu, and Chris H. Rycroft

***Abstract*—Atherosclerotic plaques are focal and tend to occur at arterial bends and bifurcations. To quantitatively monitor the local changes in the carotid vessel-wall-plus-plaque thickness (VWT) and compare the VWT distributions for different patients or for the same patients at different ultrasound scanning sessions, a mapping technique is required to adjust for the geometric variability of different carotid artery models. In this work, we propose a novel method called *density-equalizing reference map* (DERM) for mapping 3D carotid surfaces to a standardized 2D carotid template, with an emphasis on preserving the local geometry of the carotid surface by minimizing the local area distortion. The initial map was generated by a previously described arc-length scaling (ALS) mapping method, which projects a 3D carotid surface onto a 2D non-convex L-shaped domain. A smooth and area-preserving flattened map was subsequently constructed by deforming the ALS map using the proposed algorithm that combines the density-equalizing map and the reference map techniques. This combination allows, for the first time, one-to-one mapping from a 3D surface to a standardized non-convex planar domain in an area-preserving manner. Evaluations using 20 carotid surface models show that the proposed method reduced the area distortion of the flattening maps by over 80% as compared to the ALS mapping method. The proposed method is capable of improving the accuracy of area estimation for plaque regions without compromising inter-scan reproducibility.**

***Index Terms*—Area-preserving map, carotid atherosclerosis, carotid ultrasound, density-equalizing map, reference map technique, vessel-wall-plus-plaque thickness (VWT).**

I. Introduction

STROKE is a leading cause of death and disability worldwide, causing an annual mortality of nearly 133,000 in United States [1] and over 1.6 million in China [2]. Carotid atherosclerosis is a major source of emboli, which may travel and block one of the cerebral arteries, causing ischemic stroke [3]. As atherosclerosis is a focal disease with plaques predominantly occurring at bends and bifurcations (BFs) of the carotid artery, monitoring local changes in the vessel-wall-plus-plaque thickness (VWT), defined as the pointwise distance between the lumen-intima boundary (LIB) and the media-adventitia boundary (MAB) as introduced by Chiu *et al.* [4], is important for the development of sensitive biomarkers that can identify high-risk patients with rapid plaque progression in a shorter time frame. The presence of common carotid plaques was shown to be associated with a higher 5-year risk of vascular events than internal carotid plaques [5]. Therefore, monitoring the location of VWT-Change is also important for risk stratification of vascular events. Although the VWT-Change distribution for an individual patient can be visualized by mapping point-by-point measurements onto the three-dimensional carotid vessel wall, a flattened representation facilitates image analysis as clinicians can scan the entire image in a systematic manner without having to rotate and interact with the 3D surface, which may cause observers to become disoriented and losing track of which regions that had been examined and which had not [6]. More importantly, since a 3D VWT-Change map was constructed by mapping VWT-Change measurements onto the carotid surfaces, the geometry of the 3D map is highly subject-specific. For this reason, although visual matching allows for qualitative comparisons of VWT-Change distributions among subjects in placebo-controlled studies of treatment effect [7], [8] or of the same subject measured from different imaging modalities (such as 3D ultrasound and MR imaging in [9]), quantitative local comparisons were not possible without mapping the 3D distribution maps to a standardized template.

To address this issue, Chiu *et al.* [10] developed the arc-length scaling (ALS) mapping approach for mapping the 3D

Manuscript received September 18, 2019; revised December 10, 2019; accepted December 28, 2019. Date of publication January 3, 2020; date of current version August 20, 2020. The work of G. P. T. Choi was supported in part by the Croucher Foundation and in part by the Harvard Quantitative Biology Initiative and the NSF-Simons Center for Mathematical and Statistical Analysis of Biology at Harvard, award number #1764269. The work of B. Chiu was supported in part by the Research Grant Council of HKSAR Project under Grants CityU 11205917 and CityU 11203218 and in part by the City University of Hong Kong Strategic Research under Grants 7004617 and 7005226. The work of C. H. Rycroft was supported by the Applied Mathematics Program of the U.S. Department of Energy (DOE) Office of Advanced Scientific Computing Research under contract DE-AC02-05CH11231. *(Corresponding author: Gary P. T. Choi.)*

G. P. T. Choi is with the John A. Paulson School of Engineering and Applied Sciences, Harvard University, Cambridge, MA 02138 USA (e-mail: pchoi@g.harvard.edu).

B. Chiu is with the Department of Electrical Engineering, City University of Hong Kong.

C. H. Rycroft is with the John A. Paulson School of Engineering and Applied Sciences, Harvard University, and also with the Mathematics Group, Lawrence Berkeley National Laboratory.

Digital Object Identifier 10.1109/TBME.2019.2963783

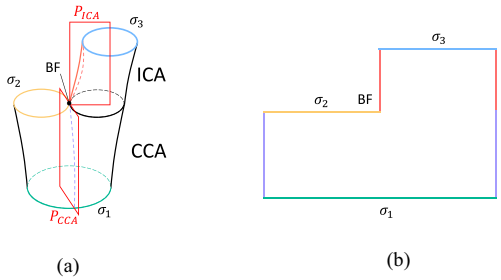

Fig. 1. An illustration of the 2D arc-length scaling (ALS) map [10] of carotid surfaces. A carotid surface is first cut by two planes, denoted by P_{ICA} and P_{CCA} (as shown in (a)), and then unfolded to a 2D L-shaped non-convex domain (as shown in (b)). The arc-length of transverse contours segmented from 2D transverse images resliced from 3D ultrasound images is rescaled such that all vertices on the carotid surface correspond to uniformly spaced grid points on the L-shaped domain. The bifurcation (denoted by BF) is mapped to the non-convex corner of the L-shaped domain, and the carotid boundaries $\sigma_1, \sigma_2, \sigma_3$ are mapped to the horizontal boundaries of the L-shaped domain. Note that if the ECA (the missing branch above σ_2 in (a)) was also included, it would appear in the top left space of the L-shaped domain in (b).

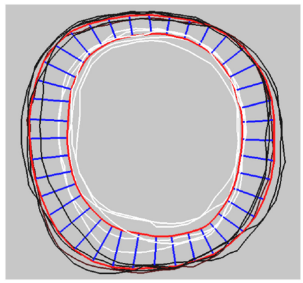

Fig. 2. Repeated segmentations of the lumen-intima boundary (LIB) and media-adventitia boundary (MAB) are represented as white and black contours respectively. The mean LIB and MAB are represented as red contours. Each blue line connect a pair of correspondence points that were matched using the symmetric correspondence algorithm [4], and the local vessel-wall-plus-plaque thickness (VWT) is the distance between each correspondence pair.

carotid surfaces onto a standardized 2D non-convex L-shaped domain (Fig. 1). Note that the external carotid artery (ECA) (i.e. the left branch above the bifurcation point) is excluded in the analysis since plaques at ECA are not directly related to stroke. The availability of the 2D standardized L-shaped carotid map has allowed for the development of sensitive biomarkers to monitor vessel wall and plaque progression/regression in clinical trials evaluating the effect of atorvastatin [10], [11] and B Vitamins [12]. However, the ALS mapping approach does not consider any local geometric distortion introduced by the 3D to 2D mapping. Unless a surface has a uniformly zero Gaussian curvature, distortion in either angle or area comes with surface flattening [13].

Conformal (angle-preserving) approaches have been proposed for flattening tubular surfaces with [14], [15] and without bifurcations [16] (see [17] for a survey). A common strategy employed in these methods was to attain conformality through solving the Dirichlet problem [18], [19]. References [14], [16] solved a longitudinal and a circumferential Dirichlet problem to generate conformal 2D maps for the colon and carotid surfaces respectively. These approaches are not suitable for carotid template construction as they generate 2D maps with shapes depending on the geometry of the original 3D surfaces. A standardized 2D map was generated by Antiga and Steinman [15] by first decomposing the common, internal and external carotid arteries (CCA, ICA and ECA) in a consistent manner based on the geometric properties at the bifurcation, resulting in three topological cylinders, each representing a carotid branch. Each carotid branch was individually mapped to a planar map (i) with longitudinal coordinates obtained by solving a Dirichlet problem and (ii) with circumferential coordinates representing the angle each carotid surface point made with the centerline. This method was implemented as an open-source software package known as the Vascular Modelling Toolkits (VMTK). Since the flattened maps for CCA, ICA and ECA were generated independently, vessel wall thickness or local hemodynamic distributions in the bifurcating region and the carotid bulb were displayed in three discontinuous sections (Fig. 4 in [15]). As plaque appears predominantly at the bifurcation and the carotid bulb, the discontinuity at these regions hampers clinical interpretation of the VWT-Change map. Moreover, since areal and volumetric measurements of plaques are related to the stroke risk of patients [20], [21] and the volume of the plaque burden can be quantified in an area-preserving flattened map, area preservation is a more important consideration than angle preservation in the development of a surface flattening approach for carotid analysis. Apart from plaque size quantification, area preservation ensures that the scope of plaque changes is accurately represented to clinicians in the flattened view of the artery.

Two area-preserving carotid flattening methods have been previously introduced [14], [22]. Zhu *et al.* [14] first computed a conformal map as described in [16] and then applied the optimal mass transport theory to correct for the area distortion exhibited in the conformal map. Chiu *et al.* [22] mapped each transverse cross-section of the carotid surface to a plane in an arc-length preserving manner and then solved the Monge-Kantorovich problem to correct for the area distortion occurred in the arc-length preserving map. This algorithm has been applied to multiple clinical studies [7], [8]. These two methods share with the two conformal maps introduced above [14], [16] in that the shape of the flattened map varies with the 3D vessel wall geometry, and therefore, not suitable for quantitative analysis of VWT-Change.

As the position and the size of plaques are two factors that have been shown to predict stroke risk [5], [21], a standardized carotid VWT-Change map should represent these two factors accurately and consistently across patients. This representation would allow these two important factors to be considered collectively for quantitative stroke risk stratification and treatment evaluation. For example, the biomarker developed previously based on the ALS map, which was able to detect the effect of Vitamin-B treatment, took into consideration the size and the position of plaque and local thickening of the vessel wall [12]. Although our previously described ALS method has attained an acceptable positional correspondence as demonstrated in an inter-scan reproducibility analysis [23], area distortion

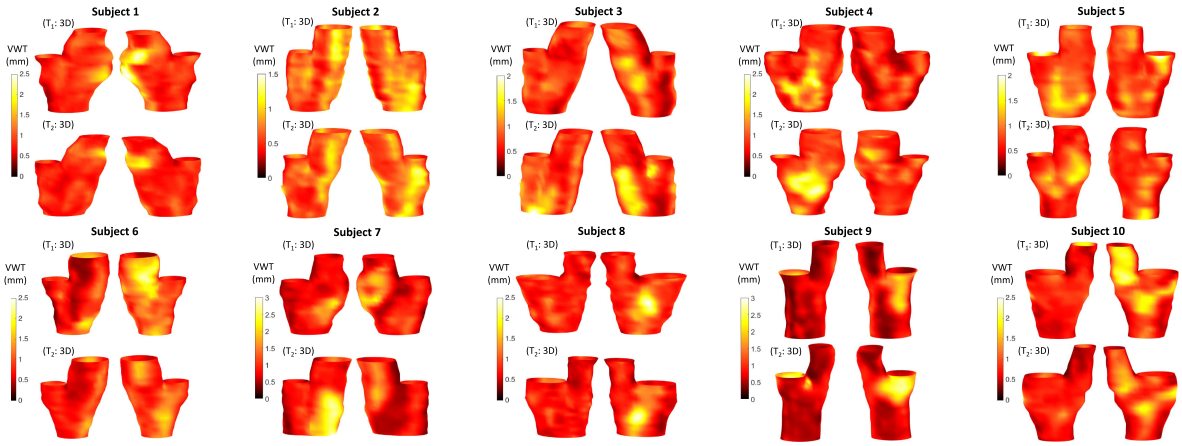

Fig. 3. The 20 3D carotid surfaces from ten subjects in our study, color-coded and superimposed by their VWT distributions (with both front and back views). For each subject, the carotid models at baseline and follow-up are labeled as T_1 and T_2 respectively.

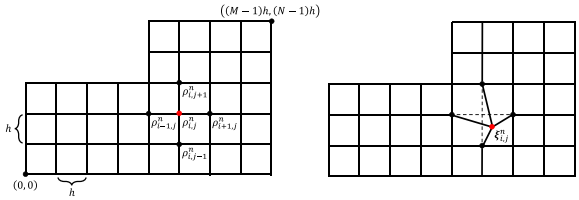

Fig. 4. Schematic for the discretization of the proposed method. On a grid with spacing h, the density $\rho^n_{i,j}$ at the grid point (ih, jh) at the n-th step is updated by solving the diffusion equation (9). Note that $\rho^n_{i,j}$ depends on the densities $\rho^n_{i\pm1,j}, \rho^n_{i,j\pm1}$ at the neighboring grid points at the n-th step, the density $\rho^{n-1}_{i,j}$ at (ih, jh) at the $(n-1)$-th step, as well as the discrete κ and its derivatives at (ih, jh). The density flux causes a velocity field (10), and the reference map $\boldsymbol{\xi}^n_{i,j}$ is updated by the advection equation (11).

generated by ALS is substantial, which may lower risk stratification accuracy and reduce the sensitivity to treatment effect. In addition, as one of the major purposes of generating the flattened map is to provide a quick comprehensive view of the entirety of plaque changes throughout the carotid bifurcation, area preservation ensures that the scope of these changes are not over or under-represented to the clinician. For these reasons, there is a need for developing an area-preserving approach for correcting the area distortion without increasing the inter-scan variability. The goal of this work is to develop and validate such a correction method.

Recently, Choi and Rycroft [24] developed a method for computing surface flattening maps by extending a technique for cartogram projection called the density-equalizing maps [25]. Although the method [24] is successful in producing an area-preserving map from a 3D surface onto a 2D domain, the bijectivity of the map is not guaranteed if the target 2D domain is non-convex. A non-bijective map has self-intersection, and in the context of VWT map construction, a point on such a map would be equipped with multiple VWT values. In other words, the VWT values at these points are not defined, which would render quantitative analysis of VWT distribution impossible. In this work, we developed and validated a novel method called *density-equalizing reference map* (abbreviated as DERM) for computing area-preserving flattening maps of carotid surfaces onto the 2D non-convex L-shaped domain, using an improved formulation of density-equalizing maps. Our method extends the idea of density diffusion for handling the non-convex corner of the L-shaped domain, and further combines it with the reference map technique [26], [27], coupling the deformation of individual nodes with the spatial information for producing a smooth and accurate mapping result. Our method produces a flattening map from 3D carotid surfaces onto a standardized non-convex 2D domain independent of the vessel geometry, with area distortion minimized, and with bijectivity ensured. To the best of our knowledge, this is the first work that is capable of achieving all these three properties for carotid flattening. The area-preserving map generated using the proposed algorithm will provide an accurate and consistent collective representation of plaque size and position that would allow unbiased quantitative comparisons of the extent of carotid diseases among patients involved in population studies.

II. Mathematical Background

A. Density-Equalizing Map

Gastner and Newman [25] proposed an algorithm for producing *density-equalizing map projections* based on a physical principle of density diffusion. Conceptually, given a planar map (such as the world atlas) and a density distribution prescribed on every part of the map, the method continuously deforms the map such that the difference in the density at different regions is transformed into a difference in the area of the regions. Regions with a larger prescribed density expand and those with a smaller density shrink. Ultimately, the density is equalized over the entire deformed map.

Mathematically, given a planar domain D and a quantity $\rho(\mathbf{x}, 0)$ called the *density* defined at every location $\mathbf{x}$ on D at time $t = 0$, the method deforms D by equalizing $\rho(\mathbf{x}, t)$ as $t \to \infty$. The equalization of ρ follows from the advection equation $\frac{\partial \rho}{\partial t} = -\nabla \cdot \mathbf{j}$, where $\mathbf{j} = -\nabla \rho$ is the diffusion flux with

uniform diffusivity. This yields the diffusion equation

$$\frac{\partial \rho}{\partial t} = \Delta \rho. \tag{1}$$

The density flux causes any tracers to move with velocity

$$\mathbf{v} = -\frac{\nabla \rho}{\rho}. \tag{2}$$

With the velocity field, the location of any tracer $\mathbf{x}$ at time t can be traced by

$$\mathbf{x}(t) = \mathbf{x}(0) + \int_0^t \mathbf{v}(\mathbf{x}(\tau), \tau) d\tau, \tag{3}$$

where τ represents the intermediate time between time 0 and time t. Taking $t \to \infty$, ρ is equalized on the entire domain, and the above displacement produces a deformed map $\mathbf{x}_{\text{final}}$ that encodes all the density difference in the original density $\rho(\mathbf{x}, 0)$ in terms of the area difference of different parts on the final deformed map $\mathbf{x}_{\text{final}}$.

The algorithm was primarily applied to the visualization of sociological data such as population and average income on the world atlas [28]. Recently, Choi and Rycroft [24] explored the close connection between density-equalizing maps and surface flattening. In particular, by setting ρ as the face area of a 3D surface mesh and computing a density-equalizing map from the 3D surface to a 2D domain, the deformation follows the ratio of the face area at different regions and hence the resulting density-equalizing map is an area-preserving map. This idea sets the stage for our area-preserving mapping method for carotid surfaces.

B. The Reference Map Technique

Rycroft, Kamrin, and colleagues [26], [27] developed the *reference map technique* for simulating large-strain solid mechanics with a fully Eulerian formulation. Suppose a body is under deformation such that the material initially located at the position $\mathbf{X}$ is moved to the position $\mathbf{x}$ at time t. $\mathbf{x}(\mathbf{X}, t)$ is a motion function which keeps track of the motion of the material initially at $\mathbf{X}$. Define the *reference map* $\mathbf{X} = \boldsymbol{\xi}(\mathbf{x}, t)$ as the inverse of the motion function. $\boldsymbol{\xi}(\mathbf{x}, t)$ can be regarded as a vector field in the deformed body which indicates the reference location of the material occupying the position $\mathbf{x}$ at time t. In particular, $\boldsymbol{\xi}(\mathbf{x}, 0) = \mathbf{x}$. Since the reference location of any tracer particle is the same at all time t under the deformation, we have $\dot{\boldsymbol{\xi}} = 0$, yielding the advection equation

$$\frac{\partial \boldsymbol{\xi}}{\partial t} + \mathbf{v} \cdot \nabla \boldsymbol{\xi} = \mathbf{0}. \tag{4}$$

By solving the above equation as $t \to \infty$, the final reference map $\boldsymbol{\xi}(\mathbf{x}_{\text{final}}, \infty)$ gives the reference location of the material occupying the final position $\mathbf{x}_{\text{final}}$ of the deformed body. Therefore, to obtain $\mathbf{x}_{\text{final}}$ from $\boldsymbol{\xi}$, we simply need to track the contour lines of the x- and y- coordinates of $\boldsymbol{\xi}$.

III. Materials and Methods

A. Study Subjects and 3D Ultrasound Image Acquisition

Ten subjects with carotid atherosclerosis were involved in this study. These subjects were recruited from The Premature Atherosclerosis Clinic and the Stroke Prevention Clinic at the London Health Science Center, London, Canada and the Stroke Prevention & Atherosclerosis Research Center, Robarts Research Institute, London, Canada. Each subject was scanned at baseline and two weeks later with a 3D ultrasound carotid imaging system, providing 20 carotid ultrasound images for the evaluation of the proposed algorithm. The reason of imaging patients 2 weeks apart was to evaluate the change in the VWT map representation stemming from variability due to patient repositioning, different neck orientations and sonographer change across the two scanning sessions [29]. The patients investigated have stable atherosclerosis and no physiological changes were expected to increase the inter-scan variability of VWT.

The 3D ultrasound carotid imaging system has been detailed previously [30] and briefly summarized here. A transducer (L12-5, Philips, Bothel, WA, USA) mounted on a mechanical assembly translated along the neck of the patient for 4 cm while contiguous 2D images were acquired by the ATL HDI 5000 ultrasound machine (Philips, Bothel, WA, USA) at regular spatial intervals of 0.15 mm. Ultrasound frames were captured and digitized by a frame grabber and reconstructed into a 3D carotid image volume.

The reconstruction of the 3D carotid surfaces and the construction of the 3D VWT map was described previously [4], [10]–[12], [22], [23], [31], [32]. The 3D images were resliced at 1 mm intervals perpendicular to the medial axis of the vessel identified by an expert observer, who then segmented the LIB and MAB of the carotid artery on each resliced image. The 3D lumen and vessel wall surfaces were subsequently reconstructed from the segmented boundary stacks. To reduce the effect of segmentation variability, the LIB and MAB were repeatedly segmented five times, with consecutive segmentation sessions separated by at least 24 hours to minimize observer memory bias. As shown in Fig. 2, segmentation of LIB and MAB was prone to observer variability. A previous analysis [10] shows that segmenting a boundary repeatedly and taking the average of the repeated segmentations reduces the variability by a factor of N, where N is the number of repeated segmentations performed. The mean LIB and MAB surfaces for each carotid artery were then computed and matched on a point-by-point basis by using the symmetric correspondence technique described in [4]. The VWT was measured by taking the distance between each pair of corresponding points (i.e., length of blue lines in Fig. 2). The 3D VWT map was constructed by superimposing this pointwise VWT on the MAB surface as previously described. Fig. 3 shows all 20 3D carotid surfaces in our study.

B. 2D Arc-length Scaling (ALS) Map

Chiu *et al.* [10] proposed the arc-length scaling (ALS) mapping method for flattening the 3D VWT map onto a 2D non-convex L-shaped domain. Here we briefly describe the method and refer readers to previous works [11], [31] for more details. The method begins with transforming the 3D carotid surface to a standard coordinate system, with the bifurcation (BF) located at the origin, the longitudinal direction of the common carotid artery (CCA) aligned with the z-axis, and the internal carotid artery (ICA) located at the upper half space of the coordinate

system. The surface is then cut by two planes (Fig. 1(a)) and unfolded to a 2D L-shaped non-convex domain (Fig. 1(b)). The ICA and the CCA are respectively mapped to the top part and the bottom part of the L-shaped domain. The arc-length of transverse contours segmented from 2D transverse images resliced from 3D ultrasound images is rescaled so that the vertices on the carotid surface correspond to uniformly spaced grid points on the L-shaped domain. With the 2D L-shaped carotid template, a more systematic comparison between the VWT of different carotid arteries can be performed.

However, the ALS mapping approach does not consider any local geometric distortion produced by the 3D to 2D mapping. To reduce the geometric distortion, we consider deforming the ALS map and generate an area-preserving 2D carotid template.

C. Area-Preserving Map via Density-Equalizing Reference Map (DERM)

Denote the 2D non-convex L-shaped domain obtained by the ALS mapping method by D. We would like to deform D based on a prescribed density distribution. Let $\rho(\mathbf{x}, t)$ be the density at the location $\mathbf{x}$ on D at time t. To achieve an area-preserving map, we set $\rho(\mathbf{x}, 0)$ to be the area of each face of the carotid surface and consider a diffusion-based deformation.

Here, we consider a more general version of the diffusion process when compared to the formulation (1) described in II-A. Consider the diffusion equation with diffusivity κ:

$$\frac{\partial \rho}{\partial t} = \nabla \cdot (\kappa \nabla \rho) = \kappa \Delta \rho + \nabla \kappa \cdot \nabla \rho. \tag{5}$$

κ is a differentiable function that we introduce for handling the non-convex corner of the L-shaped domain. To regularize the deformation around the non-convex corner, we slow down the diffusion process there by considering a differentiable function κ with $\kappa \ll 1$ around the non-convex corner and $\kappa \approx 1$ at the regions far away from it. One possible choice of such κ is

$$\kappa(x, y) = 1 - \left(1 - \frac{1}{\sqrt{a}}\right) e^{-\frac{(x-p)^2 + (y-q)^2}{\sqrt{a}}}, \tag{6}$$

where (p, q) are the coordinates of the bifurcation point on D and a is the total area of D. Note that $\nabla\kappa$ in (5) can be expressed explicitly by taking partial derivatives on (6). On the boundary edges of the L-shaped domain D, we enforce the no-flux boundary condition $\mathbf{n} \cdot \nabla \rho = 0$ where $\mathbf{n}$ is the unit outward normal, so that the diffusion occurs only within D. This ensures that the subsequent diffusion-based deformation does not change the overall shape of the L-shaped domain. With the diffusivity κ, the velocity field (2) becomes

$$\mathbf{v}(\mathbf{x}, t) = -\frac{\kappa \nabla \rho}{\rho}. \tag{7}$$

Now, from the viewpoint of the reference map technique described in II-B, we treat the L-shaped domain D as a solid body and consider its deformation under the velocity field $\mathbf{v}(\mathbf{x}, t)$ induced by the density gradient. We obtain the reference map $\boldsymbol{\xi}(\mathbf{x}, t)$ by solving the advection equation

$$\frac{\partial \boldsymbol{\xi}}{\partial t}(\mathbf{x}, t) + \mathbf{v}(\mathbf{x}, t) \cdot \nabla \boldsymbol{\xi}(\mathbf{x}, t) = \mathbf{0}. \tag{8}$$

As $t \to \infty$, the density $\rho(\mathbf{x}, t)$ is equalized over D, and the associated reference map field $\boldsymbol{\xi}(\mathbf{x}_{\text{final}}, \infty)$ is a density-equalizing reference map. If the VWT at the location $\mathbf{X}$ on the initial 2D ALS map is described by a function $T(\mathbf{X})$, then the VWT on the final area-preserving map will be given by $T(\boldsymbol{\xi}(\mathbf{X}, \infty))$. Equivalently, by considering the contour lines of constant x- and y- coordinates of $\boldsymbol{\xi}$, we obtain the final area-preserving map $\mathbf{x}_{\text{final}}$.

In the discrete case, suppose D (including the top left empty space of the L-shaped domain as shown in Fig. 1) is a rectangular grid consisting of $M \times N$ grid points, with grid spacing h in both the x-direction and the y-direction. Here the top left empty space is included just for simplicity of the discretization and can be omitted in all the subsequent computations. Let the coordinates of the grid points be (ih, jh), where $0 \le i \le M-1$ and $0 \le j \le N-1$. The diffusion equation (5), the velocity field (7) and the advection equation (8) are discretized and then solved iteratively. Denote the step size by δt, and the density at the grid point (ih, jh) at the n-th step by $\rho^n_{i,j}$. The discrete version of $\mathbf{v}$ and $\mathbf{X}$ is represented in a similar manner.

Note that κ and its derivatives κ_x, κ_y can all be easily discretized. For the diffusion equation (5), we use the central difference scheme to approximate $\nabla\rho$ and solve the equation by the implicit Euler method

$$\begin{aligned}\frac{\rho^n_{i,j} - \rho^{n-1}_{i,j}}{\delta t} = \kappa_{i,j} &\frac{\rho^n_{i+1,j} + \rho^n_{i-1,j} + \rho^n_{i,j+1} + \rho^n_{i,j-1} - 4\rho^n_{i,j}}{h^2} \\ &+ (\kappa_x)_{i,j} \frac{\rho^n_{i+1,j} - \rho^n_{i-1,j}}{2\,h} \\ &+ (\kappa_y)_{i,j} \frac{\rho^n_{i,j+1} - \rho^n_{i,j-1}}{2\,h}.\end{aligned} \tag{9}$$

The no-flux boundary condition for the diffusion equation is enforced using the following ghost node approach. At the four rectangular boundaries $(x, y) = (0, jh), ((M-1)h, jh), (ih, 0), (0, (N-1)h)$ where $0 \le i \le M-1$ and $0 \le j \le N-1$, and the two L-shaped boundaries $(x, y) = (p, jh), (ih, q)$ where $0 \le ih \le p$ and $0 \le jh \le q$, we suitably replace the terms $\rho^n_{i-1,j}$, $\rho^n_{i+1,j}$, $\rho^n_{i,j-1}$, $\rho^n_{i,j+1}$ on the right hand side in (9) by $\rho^n_{i,j}$ to ensure that there is no density flux orthogonal to the boundaries. Hence, the L-shaped domain maintains its boundary shape throughout the density equalization process. If we represent ρ^n as a column vector of size $MN \times 1$, (9) can be simplified as $\rho^n = A^{-1}\rho^{n-1}$, where A is an $MN \times MN$ matrix with $A = I - \delta t(\kappa\Delta + K_x + K_y)$, $K_x + K_y$ being the matrix representation of $\nabla\kappa \cdot \nabla$. Note that A is a sparse matrix independent of n and hence we only need to compute it once throughout the iterations.

The discretization of the velocity field (7) is achieved again using the central difference scheme

$$\begin{cases} (\mathbf{v}_x)^n_{i,j} = -\kappa_{i,j} \dfrac{\rho^n_{i+1,j} - \rho^n_{i-1,j}}{2\,h\rho^n_{i,j}}, \\ (\mathbf{v}_y)^n_{i,j} = -\kappa_{i,j} \dfrac{\rho^n_{i,j+1} - \rho^n_{i,j-1}}{2\,h\rho^n_{i,j}}. \end{cases} \tag{10}$$

The advection equation (8) for updating the reference map $\boldsymbol{\xi}(\mathbf{x}, t)$ is solved using the upwind method shown in (11) at the bottom of this page.

A schematic for the above-mentioned discretization equation (11) is shown in Fig. 4. By iteratively solving (9), (10), (11) until the density ρ is fully equalized on the entire domain, we obtain the desired density-equalizing reference map $\boldsymbol{\xi}$. To obtain the associated area-preserving map $\mathbf{x}_{\text{final}}$, we denote $\boldsymbol{\xi} = (\boldsymbol{\xi}_1, \boldsymbol{\xi}_2)$. For every grid point (ih, jh) on the initial 2D L-shaped domain obtained by the ALS mapping algorithm, where $i = 0, 1, \ldots, M-1$ and $j = 0, 1, \ldots, N-1$, the corresponding point of it in the final area-preserving map $\mathbf{x}_{\text{final}}$ is the intersection point of the contour lines $\boldsymbol{\xi}_1 = ih$ and $\boldsymbol{\xi}_2 = jh$. Note that in the discrete case, each contour line is represented as a piecewise linear curve. To check whether a line segment $\{(x_1^k, y_1^k), (x_1^{k+1}, y_1^{k+1})\}$ of a $\boldsymbol{\xi}_1$-contour intersects with a line segment $\{(x_2^l, y_2^l), (x_2^{l+1}, y_2^{l+1})\}$ of a $\boldsymbol{\xi}_2$-contour, it suffices to solve the following system of four linear equations in four unknowns x^*, y^*, t_1, t_2:

$$\begin{cases} (x_1^{k+1} - x_1^k)t_1 = x^* - x_1^k, \\ (y_1^{k+1} - y_1^k)t_1 = y^* - y_1^k, \\ (x_2^{l+1} - x_2^l)t_2 = x^* - x_2^l, \\ (y_2^{l+1} - y_2^l)t_2 = y^* - y_2^l. \end{cases} \tag{12}$$

If $t_1, t_2 \in [0, 1]$, then the two line segments intersect at (x^*, y^*). Otherwise, they do not intersect. By tracking all the intersection points of the pairwise contour lines, the area-preserving map $\mathbf{x}_{\text{final}}$ can be obtained.

As for the choice of the step size δt, note that the backward Euler scheme for the diffusion equation is unconditionally stable. Following the discussion in [24], we perform a dimensional analysis on (1) and see that an appropriate dimension of δt is (length)^2. Also, as the density diffusion process is invariant under uniform rescaling of the input density ρ, δt should be independent of the magnitude of ρ. Hence, it is desirable to have the step size in the form $\delta t = \frac{\text{std}(\rho)}{\text{mean}(\rho)} \times ac$, where c is a dimensionless constant. The convergence criterion is $\frac{\text{sd}(\rho^n)}{\text{mean}(\rho^n)} \leq \epsilon$, where ϵ is the error threshold. The algorithm is summarized in Algorithm 1.

Note that the original density-equalizing map (DEM) approach [25] iteratively solves (1) with uniform diffusivity, obtains the velocity field (2) and tracks the displacement of every tracer by (3). In the discrete case, updating each tracer by (3) requires an interpolation of the velocity field at its current location in every iteration. By contrast, the proposed DERM algorithm keeps track of the reference map field by (8), which is fully Eulerian and hence no interpolation is needed throughout the iterations. Note that DERM is capable of handling surfaces with highly irregular geometry due to severe stenosis or other circumstances. The diffusivity κ and the appropriately chosen step size δt regularize the deformation caused by a large $\nabla\rho$ and ensure the stability of the numerical scheme, thereby preventing edge collapses or mesh overlaps.

Algorithm 1: Area-preserving carotid flattening via density-equalizing reference map (DERM)

Input: A carotid surface S, the error threshold ϵ, the maximum number of iterations allowed $n_{\max}$.
Output: An area-preserving map $\mathbf{x}_{\text{final}}$ on the 2D non-convex L-shaped domain.

Compute an initial map $f : S \to \mathbb{R}^2$ onto the 2D L-shaped domain using the ALS mapping [10];
Compute the area ρ of every face of S and set ρ as the density on the L-shaped domain;
Set $\delta t = \frac{\text{std}(\rho)}{\text{mean}(\rho)} \times ac$;
Compute $A = I - \delta t(\kappa\Delta + K_x + K_y)$;
Set $n = 0$ and $\rho^0 = \rho$;
repeat
  Solve $\rho^{n+1} = A^{-1}\rho^n$;
  Compute the velocity field $\mathbf{v}$ using (10);
  Update the reference map $\boldsymbol{\xi}$ using (11);
  Update $n = n + 1$;
until $\frac{sd(\rho^n)}{mean(\rho^n)} \leq \epsilon$ *or* $n \geq n_{\max}$;
By tracking the intersections of the contour lines $\boldsymbol{\xi}_1 = ih$ and $\boldsymbol{\xi}_2 = jh$ of the density-equalizing reference map $\boldsymbol{\xi} = (\boldsymbol{\xi}_1, \boldsymbol{\xi}_2)$ for all i, j, obtain the desired map $\mathbf{x}_{\text{final}}$;

IV. Results

The 2D ALS mapping algorithm was implemented in C++. The proposed area-preserving DERM method was also implemented in C++ with OpenMP parallelization (with grid spacing $h = 1$, maximum number of iterations $n_{\max} = 500$, step size constant $c = 0.01$, error threshold $\epsilon = 10^{-3}$). The sparse linear systems were solved using the biconjugate gradient stabilized method (`BiCGSTAB`) in the C++ library Eigen. On a PC with an Intel i7-6700 K quad-core processor and 16 GB RAM, for each arterial model, the 2D ALS mapping took 1 second and the proposed DERM method took 8 seconds. The visualization and statistics were produced using MATLAB.

The first column of Fig. 5 shows the front and back views of six example 3D carotid models from three subjects with their VWT distributions color-coded and superimposed. For each subject, the carotid models at baseline and follow-up are labeled as T_1 and T_2 respectively. We flattened the 3D models onto the 2D L-shaped domain using the ALS mapping method [10] and

$$\frac{\boldsymbol{\xi}_{i,j}^n - \boldsymbol{\xi}_{i,j}^{n-1}}{\delta t} = \begin{cases} -(\mathbf{v}_x)_{i,j}^n \frac{\boldsymbol{\xi}_{i,j}^{n-1} - \boldsymbol{\xi}_{i-1,j}^{n-1}}{h} - (\mathbf{v}_y)_{i,j}^n \frac{\boldsymbol{\xi}_{i,j}^{n-1} - \boldsymbol{\xi}_{i,j-1}^{n-1}}{h} & \text{if } (\mathbf{v}_x)_{i,j}^n > 0 \text{ and } (\mathbf{v}_y)_{i,j}^n > 0 \\ -(\mathbf{v}_x)_{i,j}^n \frac{\boldsymbol{\xi}_{i+1,j}^{n-1} - \boldsymbol{\xi}_{i,j}^{n-1}}{h} - (\mathbf{v}_y)_{i,j}^n \frac{\boldsymbol{\xi}_{i,j}^{n-1} - \boldsymbol{\xi}_{i,j-1}^{n-1}}{h} & \text{if } (\mathbf{v}_x)_{i,j}^n \leq 0 \text{ and } (\mathbf{v}_y)_{i,j}^n > 0 \\ -(\mathbf{v}_x)_{i,j}^n \frac{\boldsymbol{\xi}_{i,j}^{n-1} - \boldsymbol{\xi}_{i-1,j}^{n-1}}{h} - (\mathbf{v}_y)_{i,j}^n \frac{\boldsymbol{\xi}_{i,j+1}^{n-1} - \boldsymbol{\xi}_{i,j}^{n-1}}{h} & \text{if } (\mathbf{v}_x)_{i,j}^n > 0 \text{ and } (\mathbf{v}_y)_{i,j}^n \leq 0 \\ -(\mathbf{v}_x)_{i,j}^n \frac{\boldsymbol{\xi}_{i+1,j}^{n-1} - \boldsymbol{\xi}_{i,j}^{n-1}}{h} - (\mathbf{v}_y)_{i,j}^n \frac{\boldsymbol{\xi}_{i,j+1}^{n-1} - \boldsymbol{\xi}_{i,j}^{n-1}}{h} & \text{if } (\mathbf{v}_x)_{i,j}^n \leq 0 \text{ and } (\mathbf{v}_y)_{i,j}^n \leq 0 \end{cases} \tag{11}$$

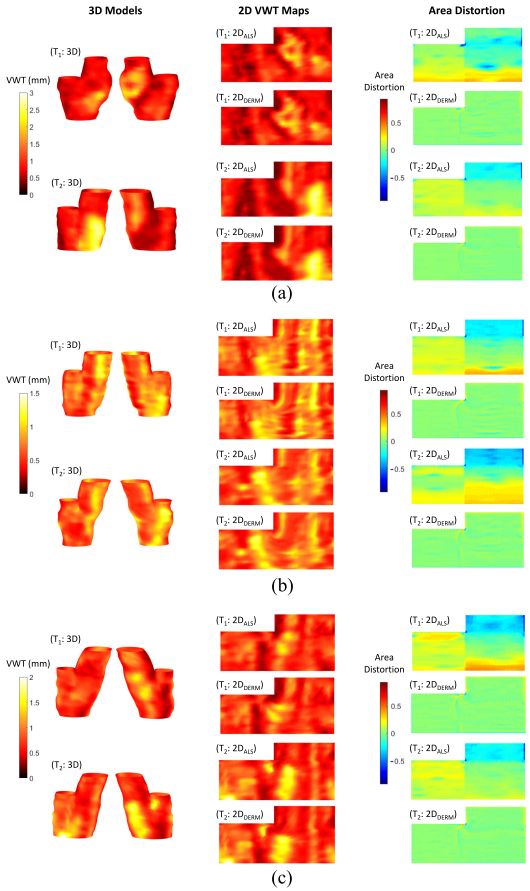

Fig. 5. Carotid flattening maps produced by the ALS mapping method [10] and our area-preserving DERM method. (a), (b), (c) show the results for three subjects. For each subject, the carotid models constructed from the baseline and follow-up 3D ultrasound images are denoted by T_1 and T_2 respectively. The first column shows the 3D carotid surfaces color-coded and superimposed by their VWT distributions (with both front and back views). The second column shows the 2D VWT maps of the carotid surfaces produced by the ALS mapping method and our area-preserving DERM method. The third column shows the area distortion maps.

our area-preserving DERM method (see the middle column of Fig. 5). Each of the 2D ALS and area-preserving flattening maps was made up of 7518 quadrilateral elements. The area distortion associated with each quadrilateral face was quantified by the logged area distortion ratio defined below:

$$d = \log_e \frac{\text{Area of the face on the flattened map}}{\text{Area of the face on the 3D carotid model}}. \quad (13)$$

A perfectly area-preserving map will result in $d = 0$ for all faces. A positive d at a local region indicates that the region is enlarged on the L-shaped 2D carotid template, while a negative d indicates that the region is shrunken. d represents enlargement and shrinkage of the same factor in an equal magnitude. For example, a face with the area halved and another with the area doubled after being flattened have $d = -0.693$ and 0.693 respectively. With this symmetric property, the logged ratio d is easier to interpret than the linear ratio. The last column of Fig. 5 shows the flattened maps with d color-coded and superimposed. In these examples, the area distortion exhibited in the ALS map was largely corrected by the proposed DERM algorithm. We

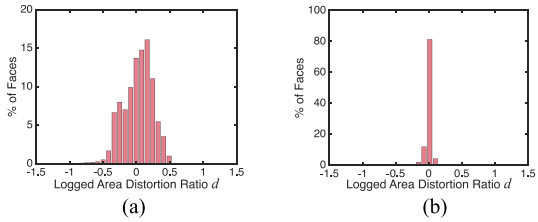

Fig. 6. Histograms of the logged area distortion ratio d exhibited in 150360 quadrilateral faces (7518 per carotid model $\times$ 20 carotid models) in (a), the 2D ALS maps and (b), the 2D area-preserving maps produced by the proposed DERM algorithm.

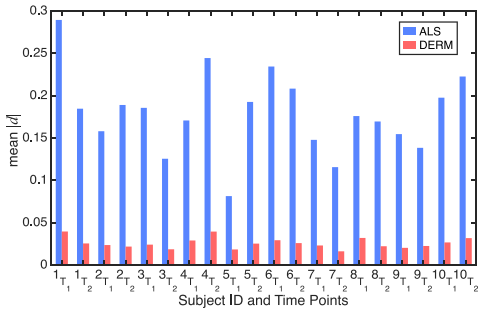

Fig. 7. Average absolute area distortion mean($|d|$) of 20 carotid models. The carotid models constructed from the baseline and follow-up 3D ultrasound images for each subject are denoted by the subscripts T_1 and T_2 respectively.

further evaluated the area distortion of the 150360 quadrilateral elements in all the 20 carotid models (7518 per carotid model $\times$ 20 models) before and after the application of the proposed algorithm. Figs. 6(a),(b) show the area distortion histogram for the ALS and the proposed algorithm, respectively. The histogram shown in Fig. 6(b) is much more concentrated at $d = 0$ than Fig. 6(a), indicating the area distortion associated with the proposed method is smaller than the ALS mapping method.

We also quantified the performance of the proposed flattening algorithm for each of the 20 carotid models by the average value of $|d|$ over the corresponding 2D maps. Fig. 7 shows the values mean($|d|$) of the 2D ALS map and the 2D area-preserving map produced by the proposed DERM method for each carotid model. The proposed method attained a reduction in area distortion by over 80% on average. A two-sample t-test shows that the average area distortion is significantly reduced by the proposed method ($P < 10^{-6}$).

In addition to minimizing area distortion, the proposed method contributed in the elimination of overlapping cells when mapping to a non-convex domain. Fig. 8 compares the performance of three methods aiming to correct the area distortion associated with ALS mapping. Figs. 8(c)–(e) show the results generated at the non-convex corner of the L-shaped domain by the density-equalizing map (DEM) [25], the shape-prescribed density-equalizing map (SPDEM) [24] and the proposed DERM method. For both DEM and SPDEM, the density was set to be the face area for computing area-preserving flattening maps. The free boundary condition in DEM was replaced by the no-flux boundary condition for enforcing the L-shape. The target boundary shape in SPDEM was also set to be the L-shape, and the method imposed the no-flux boundary condition to maintain the

TABLE I

THE AREA DISTORTION AND THE TOTAL OVERLAPPING AREA IN EACH FLATTENED MAP PRODUCED BY ALS [10], DEM [25], SPDEM [24], AND THE PROPOSED DERM METHOD. THE AREA DISTORTION WAS QUANTIFIED BY THE LOGGED AREA DISTORTION RATIO d (13), AND THE TOTAL OVERLAPPING AREA A_{OVERLAP} (IN MM^2) WAS CALCULATED BY THE DIFFERENCE BETWEEN THE SUM OF AREA OF ALL QUADRILATERAL FACES IN THE FLATTENED MAP AND THE AREA ENCLOSED BY THE BOUNDARY OF THE L-SHAPED DOMAIN

Carotid model	ALS [10]		DEM [25]		SPDEM [24]		DERM	
	mean($\lvert d\rvert$)	A_{overlap}	mean($\lvert d\rvert$)	A_{overlap}	mean($\lvert d\rvert$)	A_{overlap}	mean($\lvert d\rvert$)	A_{overlap}
Subject 1 Time 1	0.29	0	0.15	4.27	0.04	8.88	0.04	0
Subject 1 Time 2	0.18	0	0.07	1.97	0.03	4.57	0.03	0
Subject 2 Time 1	0.16	0	0.06	2.47	0.02	3.55	0.02	0
Subject 2 Time 2	0.19	0	0.06	2.43	0.03	3.03	0.02	0
Subject 3 Time 1	0.19	0	0.08	2.87	0.02	4.52	0.02	0
Subject 3 Time 2	0.13	0	0.05	2.18	0.02	3.09	0.02	0
Subject 4 Time 1	0.17	0	0.05	1.29	0.02	1.65	0.03	0
Subject 4 Time 2	0.24	0	0.09	3.01	0.03	4.82	0.04	0
Subject 5 Time 1	0.08	0	0.02	0.36	0.01	0.49	0.02	0
Subject 5 Time 2	0.19	0	0.05	1.89	0.02	2.61	0.03	0
Subject 6 Time 1	0.23	0	0.11	4.58	0.03	5.40	0.03	0
Subject 6 Time 2	0.21	0	0.08	3.19	0.03	3.39	0.03	0
Subject 7 Time 1	0.15	0	0.03	0.83	0.02	1.21	0.02	0
Subject 7 Time 2	0.12	0	0.04	1.49	0.01	2.31	0.02	0
Subject 8 Time 1	0.18	0	0.05	1.65	0.02	1.57	0.03	0
Subject 8 Time 2	0.17	0	0.06	2.97	0.02	1.57	0.02	0
Subject 9 Time 1	0.15	0	0.02	0	0.02	0.22	0.02	0
Subject 9 Time 2	0.14	0	0.02	0	0.02	0	0.02	0
Subject 10 Time 1	0.20	0	0.04	1.87	0.02	1.01	0.03	0
Subject 10 Time 2	0.22	0	0.08	3.32	0.03	1.91	0.03	0

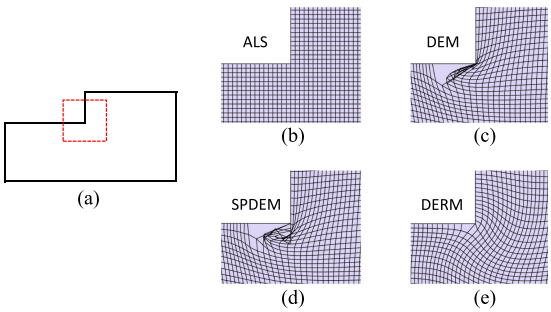

Fig. 8. Comparison between various mapping methods for handling the non-convex corner of the L-shaped domain. We consider zooming into the non-convex corner of the L-shaped domain as illustrated in (a). In (b), (c), (d), (e), the mapping results at that region produced by ALS [10], DEM [25], SPDEM [24] and the proposed DERM method are respectively shown. Our method is advantageous in adjusting for the geometric variability of the carotid surfaces without causing any overlaps.

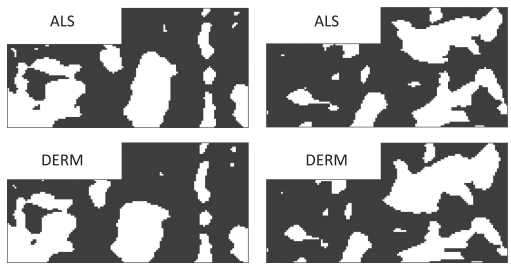

Fig. 9. Binary images of the flattened VWT maps obtained by ALS and DERM, with white representing the plaque region (i.e. with VWT $>$ 0.9 mm) and black otherwise. Each column corresponds to one carotid model.

L-shape throughout the iterations. After obtaining the flattening maps for all four methods, we checked the bijectivity of the results. It can be observed that both DEM and SPDEM produce undesirable overlaps around the non-convex corner of the L-shaped domain (Fig. 8(c),(d)) due to the large density gradient (i.e. face area difference) between the ICA and CCA generated by ALS mapping as shown in the last column of Fig. 5. Since the proposed DERM method has a non-constant diffusion coefficient κ in the diffusion process and involves the reference map technique for producing a smoother deformation, we are able to obtain an area-preserving flattening map without any overlaps (Fig. 8(e)), thereby guaranteeing bijectivity. We quantified the above observation by evaluating the total overlapping area in each flattened map, computed by taking the difference between the sum of area of all quadrilateral faces in the flattened map and the area enclosed by the boundary of the L-shaped domain. This overlap metric was computed for the entire set of 20 arteries. The mean and the standard deviation for DEM and SPDEM were 2.1 ± 1.3 and $2.8 \pm 2.1\,\text{mm}^2$ respectively. Since the proposed algorithm guarantees bijectivity, this overlap metric is 0 for all arterial models.

Table I records the average area distortion and the total overlapping area of each flattened map produced by the four above-mentioned methods. DERM achieves a significant reduction in area distortion comparable to the state-of-the-art SPDEM method and guarantees bijectivity.

A major goal of this work was to improve the accuracy of the plaque size represented in the carotid standardized map. The areas of the "plaque regions" represented in the ALS and DERM maps were compared with their corresponding areas in the 3D VWT maps. "Plaque regions" were defined as regions with VWT $>$ 0.9 mm. This threshold was chosen according to the latest European Society of Hypertension (ESH) and European Society of Cardiology (ESC) hypertension guidelines [33], which listed intimamedia thickness (IMT) $>$ 0.9 mm as a risk factor of asymptomatic organ damage. Fig. 9 shows the flattened

VWT maps constructed for two carotid models by ALS and DERM, with white representing the plaque regions and black representing the background.

The accuracy of plaque area change for each patient from baseline to follow-up obtained in the maps generated by ALS and DERM were compared with that obtained in the corresponding 3D VWT map, which was considered as the gold standard. The plaque area change errors associated with ALS and DERM mappings were computed by:

$$e_{\Delta \mathrm{PA}_i} = \Delta \mathrm{PA}_i - \Delta \mathrm{PA}_{3\mathrm{D}}, \tag{14}$$

where $i \in \{\mathrm{ALS}, \mathrm{DERM}\}$ represents the mapping method, $\Delta \mathrm{PA}_i$ denotes plaque area change estimated using method i and $\Delta \mathrm{PA}_{3\mathrm{D}}$ represents the plaque area change obtained on the 3D VWT map. For the 10 subjects involved in this study, $|e_{\Delta \mathrm{PA}_{\mathrm{ALS}}}| = 13.8 \pm 24.9\,\mathrm{mm}^2$ and $|e_{\Delta \mathrm{PA}_{\mathrm{DERM}}}| = 7.2 \pm 12.9\,\mathrm{mm}^2$. The mean error was reduced by 48% and the difference was statistically significant ($P = 0.01$).

The purpose of the above analysis was to demonstrate the significance of the reduction of the error in plaque size representation attributed by DERM. The 2D carotid template described herein integrates plaque size and positional information and allows for the development of biomarkers capable of sensitive detection of small treatment effect by dietary supplements, such as that reported in [12]. Although the above analysis involved only plaque size estimation, the 2D template should not be considered solely as a tool for plaque size estimation. Instead, if the plaque size is more accurately represented in the map, biomarkers developed from the carotid template aiming to detect treatment effect, such as that described in [12], may become more sensitive, which would further reduce the sample size required for showing the efficacy of a treatment.

The strength of the proposed 2D standardized representation of VWT is that two major determinants of stroke risk, the location and the size of plaques [5], [20], [21], can be considered collectively in quantitative analyses. Although DERM has reduced the error in plaque region area estimation as shown above, a concern would be whether the deformation involved in DERM would negatively affect anatomic correspondence. The difficulty of evaluating anatomic correspondence for carotid arteries is that there is no anatomic landmark that can be dependent upon in such an evaluation, other than the bifurcation point. By the construction of ALS, we have already ensured the bifurcation points of all arteries were mapped to a common point in the 2D carotid template. As no physiological change was expected for patients involved in this study between the two scanning sessions, inter-scan variability quantified by ΔVWT between the two sessions can be used as a metric for anatomic correspondence. A previous study using the same data set has established that ALS mapping provides good anatomic correspondence [23]. For this reason, ΔVWT associated with ALS mapping can be used as a benchmark for comparison. ΔVWTs associated with ALS and DERM were compared based on the following three parameters: (a) Percentage of points with $\Delta\mathrm{VWT} \leq 0.35\,\mathrm{mm}$ for each subject, (b) Visual comparison between the mean ΔVWT maps generated by ALS and DERM for the ten subjects involved in this study, and (c) Mean $|\Delta\mathrm{VWT}|$ for each subject.

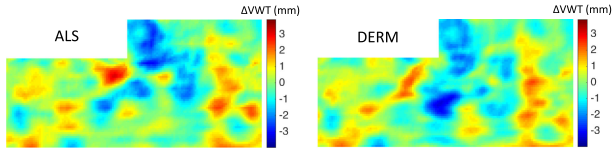

Fig. 10. The average ΔVWT map between the baseline and the follow-up generated by ALS and DERM for the ten subjects.

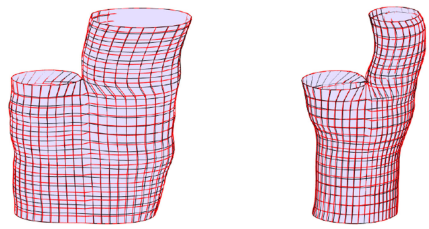

Fig. 11. The carotid models of two subjects (subjects 7 and 9) at follow-up (the black grid and the purple quads) overlaid with those at baseline (the red grid) using the point correspondence established by the 2D L-shaped domain via DERM. For better visualization, only part of the grid lines are shown.

The threshold of 0.35 mm was chosen for the following reason. The axial, lateral and elevational resolutions of our 3D imaging system are 0.6, 0.8 and 2 mm, respectively, at the depth of 40 mm, which is approximately the depth of the carotid artery [34]. The average in-plane resolution is 0.7 mm and half of which (i.e., 0.35 mm) can be considered as a "small change. This area percentage was $80.7\% \pm 6.7\%$ for ALS and $80.9\% \pm 6.4\%$ for DERM. A two-sample paired t-test shows no significant difference between the two mapping techniques ($P = 0.85$). Fig. 10 shows the average ΔVWT map between the baseline and the follow-up generated by ALS and DERM for all subjects. It can be observed that the two ΔVWT patterns are similar. The two-sample paired t-test shows no significant difference between the subject-based mean of $|\Delta\mathrm{VWT}|$ for the ten subjects by the two mapping techniques ($P = 0.80$). These results show that DERM is capable of improving the accuracy of plaque area change estimation in terms of (14) without compromising inter-scan reproducibility.

The effect of DERM area correction operation on point correspondence was further evaluated by assessing how much the 2D grids generated by ALS were deformed. The DERM-deformed grids on the 2D baseline (T_1) and follow-up (T_2) maps of the same subject were mapped to the 3D carotid surface constructed from the follow-up scan. The baseline (red) and follow-up (black) grids generated for each of the two example subjects were superimposed to allow comparison in Fig. 11. The similarity of the red and black grids shows that the deformation by DERM does not have a substantial effect in point correspondence.

V. Discussion

Density-equalizing maps [25] have been widely used in sociological data visualization and was recently introduced for the computation of area-preserving surface mapping [24]. However, the bijectivity of the maps obtained by these methods is only guaranteed when the maps are with free boundary constraints or

with a convex target shape. To overcome this limitation so as to produce area-preserving maps with the non-convex L-shape, we extended the formulation of density diffusion in these methods to allow for a non-constant diffusivity that effectively regularizes the density gradient around the non-convex corner. Note that while our algorithm was developed with a quadrilateral-based discretization of the 3D carotid models, it is also applicable to surfaces with triangle or other polygonal elements, for which the finite difference discretization in (9), (10), (11) should be replaced by the relevant triangle/polygon-based discretizations. Besides, the proposed technique is not limited by the choice of the surface reconstruction method employed. For 3D carotid surfaces reconstructed using any other methods, the proposed technique can also be applied for computing the area-preserving flattening map. We tested our algorithm with different number of surface mesh nodes n, keeping all other parameters fixed. The result shows an $O(n^{1.5})$ time scaling for each timestep, consistent with the expected scaling for the BiCGSTAB method. As for the expected rate of slow down, we have $\lim_{n\to\infty} \frac{\|\rho^{n+1}-\text{mean}(\rho)\|_2}{\|\rho^{n}-\text{mean}(\rho)\|_2} = 1$ and $\lim_{n\to\infty} \frac{\|\rho^{n+1}-\rho^{n}\|_2}{\|\rho^{n}-\rho^{n-1}\|_2} = 1$, indicating that the process converges logarithmically.

Another limitation of the previous methods is that the deformation of each node on the domain was tracked individually without considering the neighboring spatial information, which results in an unsmooth mapping result under a large deformation. The reference map technique [26], [27] was originally developed for tracking large physical deformations of a solid body smoothly. For the first time, the reference map technique was integrated with the density-equalization process to generate a smooth and area-preserving flattened map. Although this technique was applied on carotid mapping, it can be applied to facilitate the interpretation of spatial distributions on the surfaces of other organs, such as brain ventricles and kidneys [35]. Carotid mapping described in this paper is particularly challenging due to the non-convex nature of the carotid template. A highlight of the proposed algorithm is that it allows bijective (one-to-one) mapping even at the non-convex corner at the carotid bifurcation, whereas previous density-equalizing approaches do not guarantee bijectivity in a non-convex domain (Fig. 8).

The proposed algorithm shares with previous area-preserving algorithms [14], [22] that the area distortion could not be completely eliminated, although the method reduced the area distortion in a statistically significant manner. This limitation can be explained by the finite grid size and step size used in our numerical scheme. A possible way to further reduce the area distortion without slowing down the computation is to extend our algorithm with an adaptive framework, which will allow us to take adaptive time steps to handle specific regions with relatively large distortion. This strategy will be implemented and our hypothesis will be validated in a future investigation.

In this work, we set the density ρ to be the local 3D surface area of the artery so that density-equalization gives us an area-preserving map. We can extend our method to take tissue properties into account by setting ρ to be equal to $\frac{\text{Local surface area}}{\text{Young's modulus}}$. In this setting, if a region is calcified and more rigid (with larger Young's modulus), a smaller area change is allowed, while if the region is healthy and more flexible (with lower Young's modulus), a larger area change can be accommodated in the resulting map.

Although this algorithm was applied in analyzing 3D carotid ultrasound images, the proposed method is equally applicable to any imaging modality that allows the segmentation of the LIB and MAB. In fact, an earlier version of the carotid flattening approach [22] has been used in comparing the vessel wall thickness measured from 3D ultrasound and MRI [9]. As mentioned in the introduction, the shape of the 2D carotid map generated by the algorithm proposed in [22] was not standardized. Therefore, only a qualitative comparison was possible by matching the 3D ultrasound and MRI maps visually. The standardized carotid map currently available would allow for quantitative comparisons of the VWT measured from the two imaging modalities. In the past 10–15 years, many clinical trials have been performed to evaluate the feasibility of using carotid vessel wall MRI to detect the effect of lipid-lowering therapies [36]–[39]. The outcomes of these trials were evaluated in terms of global parameters, such as vessel wall area and maximum wall thickness. The ability to analyze the VWT distribution quantitatively afforded by the proposed approach may allow for more sensitive detection of treatment effect.

Besides, although the density-equalizing approach introduced here was used to generate area-preserving carotid maps, its application can be extended to non-rigid carotid registration (i.e. finding an optimal deformation to match carotid images). 3D ultrasound images are acquired at baseline and a follow-up imaging session in serial monitoring of the carotid disease. Even if no physiological changes are expected, such as in the case where patients are presented with stable disease and the time interval between the baseline and follow-up imaging session is as short as two weeks [7], there would be variance in the VWT maps due to different patient position and neck orientation that could only be corrected by non-rigid registration techniques. The proposed pipeline can be extended in the future and used for registering VWT maps obtained in the two imaging sessions in a non-rigid manner. However, one will need to replace the density-equalizing velocity field by a suitable velocity field that provides a descent direction for reducing the VWT difference between the two maps before this framework can be extended to be used in non-rigid registration. The improved reproducibility of the VWT maps thus produced may play a role in increasing the sensitivity of biomarkers that quantify the change in VWT distribution for evaluation of new therapies. One example of such biomarker is the mutual-information-weighted biomarker used to quantify the weighted VWT-Change average exhibited in a one-year longitudinal study involving patients who received placebo and Vitamin B tablets [12]. Although a statistically significant difference was found between the two treatment groups, thereby establishing the effect of Vitamin-B treatment on atherosclerosis, only rigid registration was performed to align the arteries imaged at baseline and the follow-up session before the construction of VWT maps. The non-rigid registration capability of the proposed algorithm has the potential to further increase the sensitivity of the biomarkers characterizing VWT-Change. Such an improvement would reduce the sample size required to establish effects of

new medical treatments on atherosclerosis, thereby increasing the cost-effectiveness of clinical trials.

VI. Conclusion

In this work, we have proposed a novel method for producing area-preserving flattening maps for visualization and consistent quantification of the VWT distributions on carotid surfaces. Our method first takes the 2D L-shaped non-convex domain produced by the ALS mapping algorithm [10] as an initial map. Then, we improved the density diffusion process [24], [25] and combined it with the reference map technique [26], [27]. From the experimental results, it can be observed that the area distortion of the flattening maps was significantly reduced by our proposed method. The bijectivity at the non-convex corner of the L-shaped domain was also guaranteed by the nonconstant diffusivity in the density equalization process. Our method provides an accurate and consistent way for flattening 3D carotid models onto a standardized 2D template for carotid analysis, with the geometric variability of them taken into account. The experimental results have demonstrated the capability of our method for reducing the plaque size representation error without compromising inter-scan reproducibility. The improved collective representation of plaque size and position in the proposed standardized 2D carotid template will allow for unbiased quantitative comparisons in population studies.

References

[1] E. J. Benjamin, "Heart disease and stroke statistics–2017 update: A report from the american heart association," *Circulation*, vol. 135, pp. e146–e603, 2017.

[2] L. Liu *et al.*, "Stroke and stroke care in china: Huge burden, significant workload, and a national priority," *Stroke*, vol. 42, pp. 3651–3654, 2011.

[3] B. M. Eicke, J. V. Lorentz, and W. Paulus, "Embolus detection in different degrees of carotid disease," *Neurological Res.*, vol. 17, pp. 181–184, 1995.

[4] B. Chiu *et al.*, "Quantification of carotid vessel wall and plaque thickness change using 3D ultrasound images," *Med. Phys.*, vol. 35, pp. 3691–3710, 2008.

[5] S. Prabhakaran *et al.*, "Carotid plaque surface irregularity predicts ischemic stroke: The northern manhattan study," *Stroke*, vol. 37, pp. 2696–2701, 2006.

[6] M. Borkin *et al.*, "Evaluation of artery visualizations for heart disease diagnosis," *IEEE Trans. Vis. Comput. Graph.*, vol. 17, no. 12, pp. 2479–2488, Dec. 2011.

[7] M. Egger *et al.*, "Mapping spatial and temporal changes in carotid atherosclerosis from three-dimensional ultrasound images," *Ultrasound Med. Biol.*, vol. 34, pp. 64–72, 2008.

[8] A. Krasinski *et al.*, "Three-dimensional ultrasound quantification of intensive statin treatment of carotid atherosclerosis," *Ultrasound Med. Biol.*, vol. 35, pp. 1763–1772, 2009.

[9] A. Krasinski *et al.*, "Magnetic resonance imaging and three-dimensional ultrasound of carotid atherosclerosis: Mapping regional differences," *J. Magn. Reson. Imag.*, vol. 29, pp. 901–908, 2009.

[10] B. Chiu, B. Li, and T. W. S. Chow, "Novel 3D ultrasound image-based biomarkers based on a feature selection from a 2D standardized vessel wall thickness map: A tool for sensitive assessment of therapies for carotid atherosclerosis," *Phys. Med. Biol.*, vol. 58, pp. 5959–5982, 2013.

[11] B. Chiu, W. Chen, and J. Cheng, "Concise biomarker for spatial-temporal change in three-dimensional ultrasound measurement of carotid vessel wall and plaque thickness based on a graph-based random walk framework: Towards sensitive evaluation of response to therapy," *Comput. Biol. Med.*, vol. 79, pp. 149–162, 2016.

[12] J. Cheng *et al.*, "Sensitive three-dimensional ultrasound assessment of carotid atherosclerosis by weighted average of local vessel wall and plaque thickness change," *Med. Phys.*, vol. 44, pp. 5280–5292, 2017.

[13] M. S. Floater and K. Hormann, "Surface parameterization: A tutorial and survey," in *Proc. Advances Multiresolution Geometric Modelling*, 2005, pp. 157–186.

[14] L. Zhu, S. Haker, and A. Tannenbaum, "Flattening maps for the visualization of multibranched vessels," *IEEE Trans. Med. Imag.*, vol. 24, no. 2, pp. 191–198, Feb. 2005.

[15] L. Antiga and D. A. Steinman, "Robust and objective decomposition and mapping of bifurcating vessels," *IEEE Trans. Med. Imag.*, vol. 23, no. 6, pp. 704–713, Jun. 2004.

[16] S. Haker *et al.*, "Nondistorting flattening maps and the 3-D visualization of colon CT images," *IEEE Trans. Med. Imag.*, vol. 19, no. 7, pp. 665–670, Jul. 2000.

[17] J. Kreiser *et al.*, "A survey of flattening-based medical visualization techniques," *Comput. Graph. Forum*, vol. 37, pp. 597–624, 2018.

[18] S. Angenent *et al.*, "On the Laplace-Beltrami operator and brain surface flattening," *IEEE Trans. Med. Imag.*, vol. 18, no. 8, pp. 700–711, Aug. 1999.

[19] P. T. Choi, K. C. Lam, and L. M. Lui, "Flash: Fast landmark aligned spherical harmonic parameterization for genus-0 closed brain surfaces," *SIAM J. Imag. Sci.*, vol. 8, pp. 67–94, 2015.

[20] J. D. Spence *et al.*, "Carotid plaque area: A tool for targeting and evaluating vascular preventive therapy," *Stroke*, vol. 33, pp. 2916–2922, 2002.

[21] T. Wannarong *et al.*, "Progression of carotid plaque volume predicts cardiovascular events," *Stroke*, vol. 44, pp. 1859–1865, 2013.

[22] B. Chiu *et al.*, "Area-preserving flattening maps of 3D ultrasound carotid arteries images," *Med. Image Anal.*, vol. 12, pp. 676–688, 2008.

[23] Y. Chen and B. Chiu, "Correspondence optimization in 2D standardized carotid wall thickness map by description length minimization: A tool for increasing reproducibility of 3D ultrasound-based measurements," *Med. Phys.*, vol. 43, pp. 6474–6490, 2016.

[24] G. P. T. Choi and C. H. Rycroft, "Density-equalizing maps for simply connected open surfaces," *SIAM J. Imag. Sci.*, vol. 11, pp. 1134–1178, 2018.

[25] M. T. Gastner and M. E. J. Newman, "Diffusion-based method for producing density-equalizing maps," *Proc. Natl. Acad. Sci. U.S.A.*, vol. 101, pp. 7499–7504, 2004.

[26] K. Kamrin, C. H. Rycroft, and J.-C. Nave, "Reference map technique for finite-strain elasticity and fluid–solid interaction," *J. Mech. Phys. Solids*, vol. 60, pp. 1952–1969, 2012.

[27] B. Valkov, C. H. Rycroft, and K. Kamrin, "Eulerian method for multiphase interactions of soft solid bodies in fluids," *J. Appl. Mech.*, vol. 82, 2015, Art. no. 041011.

[28] D. Dorling, M. Newman, and A. Barford, *The Atlas of the Real World: Mapping the Way we Live*, Thames & Hudson, 2010.

[29] M. Egger *et al.*, "Validation of 3d ultrasound vessel wall volume: An imaging phenotype of carotid atherosclerosis," *Ultrasound Med. Biol.*, vol. 33, pp. 905–914, 2007.

[30] A. Landry *et al.*, "Manual planimetric measurement of carotid plaque volume using three-dimensional ultrasound imaging," *Med. Phys.*, vol. 34, pp. 1496–1505, 2007.

[31] B. Chiu *et al.*, "Quantification and visualization of carotid segmentation accuracy and precision using a 2D standardized carotid map," *Phys. Med. Biol.*, vol. 58, pp. 3671–3703, 2013.

[32] G. P. T. Choi *et al.*, "Conformal mapping of carotid vessel wall and plaque thickness measured from 3d ultrasound images," *Med. Biol. Eng. Comput.*, vol. 55, pp. 2183–2195, 2017.

[33] G. Mancia *et al.*, "2013 ESH/ESC guidelines for the management of arterial hypertension: The task force for the management of arterial hypertension of the european society of hypertension (ESH) and of the european society of cardiology (ESC)," *J. Hypertens.*, vol. 31, pp. 1281–1357, 2013.

[34] J. E. Browne *et al.*, "Objective measurements of image quality," *Ultrasound Med. Biol.*, vol. 30, pp. 229–237, 2004.

[35] R. H. Davies *et al.*, "3D statistical shape models using direct optimisation of description length," in *Proc. Euro. Conf. Comput. Vision*. Springer, 2002, pp. 3–20.

[36] T. Y. Tang *et al.*, "The atheroma (atorvastatin therapy: Effects on reduction of macrophage activity) study: Evaluation using ultrasmall superparamagnetic iron oxide-enhanced magnetic resonance imaging in carotid disease," *J. Am. Coll. Cardiol.*, vol. 53, pp. 2039–2050, 2009.

[37] J. M. Lee *et al.*, "Effects of high-dose modified-release nicotinic acid on atherosclerosis and vascular function: A randomized, placebo-controlled, magnetic resonance imaging study," *J. Amer. College Cardiol.*, vol. 54, pp. 1787–1794, 2009.

[38] A. Varghese *et al.*, "Effect of rosiglitazone on progression of atherosclerosis: Insights using 3D carotid cardiovascular magnetic resonance," *J. Cardiovasc. Magn. Reson.*, vol. 11, pp. 1–9, 2009.

[39] K. Miyauchi *et al.*, "Rationale and design of the carotid plaque in human for all evaluations with aggressive rosuvastatin therapy (challenger trial)," *Circ. J.*, vol. 73, pp. 111–115, 2009.